Journal of Chromatography A 1785 (2026) 467325

Contents lists available at ScienceDirect

Journal of Chromatography A

journal homepage: www.elsevier.com/locate/chroma

A modeling framework for uncertainty quantification in filter-plate-based high-throughput screening of the chromatography partition coefficient

Jan Faessler [a,b], Emmy Schiess [b], Rudger Hess [b], Till Briskot [b], Sebastian Andris [b], Melanie Maier [b], Jan-Hendrik Huth [b], Joey Studts [b], Jürgen Hubbuch [a,*]

[a] Karlsruhe Institute of Technology (KIT), Institute of Engineering in Life Sciences, Section IV: Biomolecular Separation Engineering, Karlsruhe, Germany
[b] Global Development CMC Biologicals, Boehringer Ingelheim Pharma GmbH & Co. KG, Biberach, Germany

ARTICLE INFO

Keywords:
mAb
IEX
POROS XS
Chromatography partition coefficient (Kp)
High-throughput screening
Uncertainty quantification
Monte Carlo

ABSTRACT

High-throughput screening (HTS) of chromatography partition coefficients (K_p) is widely used in protein purification process development, spanning applications with markedly different precision requirements. Despite this widespread use, quantitative guidance on how experimental uncertainty propagates through filter-plate-based K_p assays and informs key design decisions has been lacking.

We present an experimentally calibrated Monte Carlo (MC) framework for uncertainty propagation in filter-plate-based K_p HTS, which quantifies overall uncertainty and identifies the dominant experimental error sources across purification-relevant equilibrium regimes. The model is parameterized by characterization of the major sources of experimental errors in a monoclonal antibody (mAb) monomer case study on POROS XS cation-exchange media and accurately reproduces the magnitude, heteroscedasticity, and plate-to-plate variability observed.

Variance decomposition identifies uncertainty in resin slurry distribution and supernatant concentration measurements as the dominant contributors, accounting for ≈ 97 % of total K_p variance over the investigated range of ideal partition coefficients ($K_{p,ideal}$). The framework further enables quantitative evaluation of design choices: analysis of the liquid-to-solid phase ratio (β) reveals a clear trade-off between measurement precision and protein material demand, allowing derivation of application-specific phase ratio recommendations.

Overall, this work provides a quantitative basis for uncertainty-aware HTS design and more reliable K_p data for purification process development decisions and modeling.

1. Introduction

In the early stages of biopharmaceutical purification process development, typically only limited information is available regarding the target protein, its impurity profile, and the concentrations of these species. At the same time, initiatives such as Quality by Design (QbD) [1] and Speed to Clinic [2] call for systematic and efficient development strategies. The increasing complexity of emerging therapeutic modalities further reduces the reliability of experience-based process design alone [3]. To address these challenges, high-throughput techniques, enabled by their high level of miniaturization, automation, and parallelization, are widely employed to explore a broad range of process conditions [4,5]. Since chromatographic unit operations remain pivotal to biopharmaceutical manufacturing [6], high-throughput process development (HTPD) commonly relies on batch partition experiments to assess the adsorptive behavior of product–impurity combinations with respect to kinetics [7], separability [8] and capacity [9] under varying buffer and resin conditions. High-throughput screening (HTS) of the chromatography partition coefficient (K_p) offers an efficient way to identify favorable separation conditions, making it a valuable criterion for identifying promising purification strategies [10,11].

However, establishing HTS for K_P determination remains challenging due to the large number of available options in experimental design and the highly application-dependent precision requirements across different HTS use cases. The strengths and weaknesses of various experimental designs have been reviewed extensively [5,12–15] and therefore need to be considered in the context of equipment availability. A foundational contribution in this regard is the publication by Coffman et al. [16], which proposes the use of filter plates and discusses the influence of liquid pipetting, resin pipetting, binding kinetics, hold-up

* Corresponding author.
E-mail address: juergen.hubbuch@kit.edu (J. Hubbuch).

https://doi.org/10.1016/j.chroma.2026.467325
Received 20 May 2026; Received in revised form 31 July 2026; Accepted 3 August 2026
Available online 4 August 2026

corrections, and analytical methods on the outcome of the HTS. Complementary to the aspects highlighted by Coffman et al., literature also places strong emphasis on the accurate definition of liquid-solid phase ratios and the precision of analytical readouts. Lacki and Brekkan [17] demonstrated the substantial impact that errors in dispensed chromatography media and concentration measurements can have on calculated K_p values. In line with this, Bergander and Lacki [18] underline the importance of correctly defined and controlled phase ratios to enable meaningful comparisons across chromatography media and process conditions. Consequently, substantial effort in the literature has focused on ensuring accurate and consistent delivery of chromatography media to every well. Building on a device introduced by Herrmann et al. [19] to establish equally sized particle plaques, subsequent studies proposed approaches for robust resin-slurry dispensing [20] and in-line resin quantification [21]. Alternatively, Li et al. [22] demonstrated that self-packed filter-plates can be prepared using a liquid-handling station (LHS) instead of resin plaques, yielding ready-to-use formats suitable for purification process development.

Although considerable effort has gone into identifying specific sources of experimental variation, the rise of automated experimentation has intensified the need to understand how these sources jointly propagate through HTS workflows. As highlighted by Wiechert et al. [23], uncertainty quantification is essential for building trust in automated experimentation, since automation accelerates data generation but simultaneously amplifies noise and complexity. Clarifying how different factors influence experimental outcomes enables more robust and efficient process-development decisions. Moreover, quantifying uncertainty can help to reduce the need for experimental replicates, thereby increasing throughput, conserving time and materials – resources that are particularly limited in early development stages. Ultimately, such methodological rigor strengthens data integrity, ensuring that modeling-based approaches are grounded in trustworthy information, paving the way towards AI-guided process development [24]. In this context, recent studies establishing quantitative structure-property relationship (QSPR) models for K_p exemplify the strong potential of high-quality HTS data to deepen mechanistic understanding of adsorption phenomena and accelerate chromatographic process development [25,26].

General guidelines for the estimation of measurement uncertainty are provided by the Joint Committee for Guides in Metrology (JCGM) [27], and are increasingly applied in life sciences. Common approaches include Gaussian error propagation, Bayesian inference, and Monte Carlo (MC) methods [28–33]. MC sampling is particularly suitable for automated workflows as it can handle nonlinearity and arbitrary distributions with conceptual simplicity, making it a robust choice for high-throughput settings [23]. Osberghaus et al. [34] demonstrated that MC sampling is an appropriate method for uncertainty quantification in high-throughput workflows. In their study, MC-based simulations were applied to 96-well plate experiments for isotherm determination under a single condition, demonstrating the method's robustness in propagating errors arising from pipetting, plaque volume, and stock solution preparation. Kittelmann et al. [21] extended the application of MC simulations to a high-throughput batch screening process in 384-well plates for isotherm determination. Their study showed that the accuracy of Langmuir parameter estimation strongly depends on the number of data points, thereby confirming that MC methods are an effective tool for analyzing error propagation in miniaturized workflows. To date, no experimentally calibrated and validated framework exists that simultaneously quantifies total uncertainty in filter-plate-based K_p HTS and resolves parameter-specific error contributions across the relevant equilibrium range, which is a prerequisite for understanding and controlling uncertainty in both process development decisions and uncertainty-sensitive modeling applications.

In this study, we established an MC-based uncertainty modeling framework for filter-plate-based K_p high-throughput screening to quantify measurement variability and distinguish the contributions of the dominant error sources across ideal partition equilibria relevant to early purification process development. To provide realistic model inputs, we experimentally characterized the distributions of the dominant variability drivers. The modeling framework was validated in a case study using the cation-exchange (CEX) resin POROS XS and a monoclonal antibody (mAb) monomer, where simulated uncertainty was compared directly to observed variability at plate and replicate levels. Based on the validated model, we quantified the relative contribution of individual parameters to total K_p variance, and derived workflow-specific guidance for improving precision. Finally, we examined phase ratio design to quantify the trade-off between measurement precision and protein demand, enabling actionable recommendations for the rational design and optimization of filter-plate-based K_p HTS.

2. Theory and model development

2.1. Determination of K_p in filter-plate-based high-throughput screening

In protein liquid chromatography, adsorption isotherms provide essential insight into the interactions of solutes with the stationary phase. The initial slope of the isotherm defines K_p and serves as an important metric for comparing buffer conditions and chromatography resins, thereby guiding early process design [8,11,35,36]. K_p is defined as follows:

$$K_p = \lim_{c \to 0} \frac{q}{c} \tag{1}$$

where q and c denote the equilibrium concentrations of the stationary and mobile phase, respectively, with q expressed per settled bed volume. The determination of K_p from batch binding equilibria has a long history and has significantly improved in throughput with the advent of automated LHS [37,38]. Furthermore, the use of filter-plates facilitates removal of the liquid phase, enabling conditioning prior to protein loading [12,16]. Measuring the concentration of the evacuated supernatant, c_{sup}, enables the calculation of the stationary phase concentration via a mass balance over the working volume. Assuming no protein is initially bound to the resin, Eq. (2). follows directly:

$$q = \frac{V_L\ c_L - (V_L + V_H)\ c_{sup}}{V_R} \tag{2}$$

Here, V_L denotes the pipetted liquid volume, c_L the load concentration, V_H the hold-up volume after centrifugation following the equilibration phase, and V_R the resin volume. In this study, the resin volume is defined by measurement of the settled-bed volume. An overview of the experimental workflow is presented in Fig. 1, with a detailed description provided in Section 3.4. As recently demonstrated by Ram et al. [39], V_R and V_H display a linear relationship, which can be expressed as Eq. (3):

$$V_H = \varepsilon_b\ V_R + V_F \tag{3}$$

where V_F denotes the liquid hold-up volume associated with the filter-plate frit, and ε_b represents the fraction of the total settled bed volume that accounts for liquid hold-up, hereafter referred to as batch hold-up porosity. Consequently, ε_b is a fraction of the total porosity (ε_t) in the centrifuged resin bed depending on the centrifugation conditions applied. Combining Eqs. (1)–(3) yields the following expression, which describes K_p as a function of the experimental design parameters and the measured c_{sup}:

$$K_p = \frac{V_L}{V_R}\left(\frac{c_L}{c_{sup}} - 1\right) - \frac{V_F}{V_R} - \varepsilon_b \tag{4}$$

The ratio V_L/V_R is often expressed as the phase ratio β, but this substitution is omitted here to maintain parameter independence in the model.

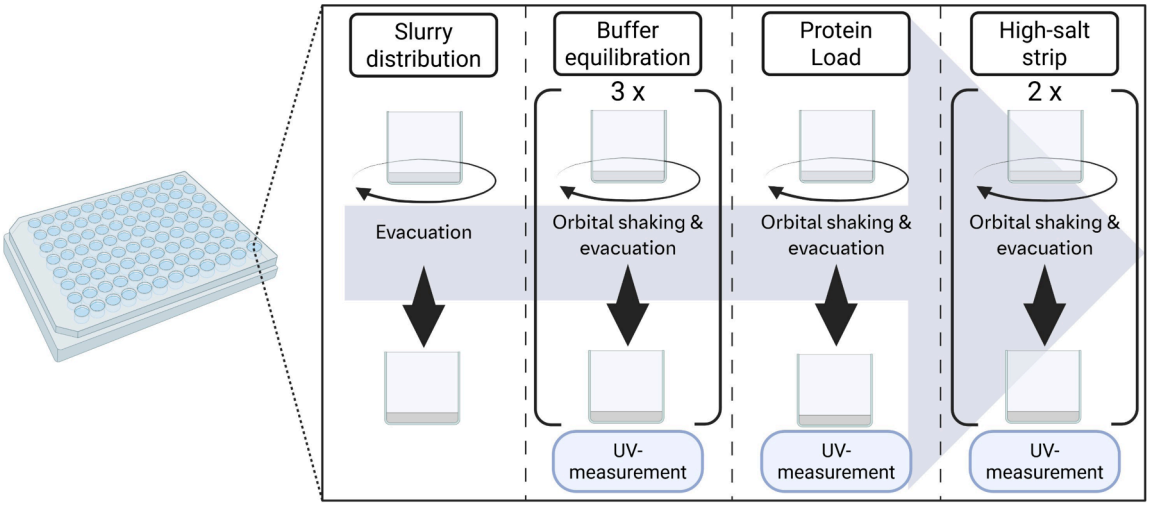

Fig. 1. Schematic overview of the experimental workflow for the filter-plate-based high-throughput screening of the chromatography partition coefficient.

2.2. Modeling measurement errors

This study introduces a method for modeling HTS-related uncertainty for a given ideal partition coefficient $K_{\mathrm{p,ideal}}$, which denotes the error-free equilibrium partition coefficient determined solely by the protein, buffer, resin and phase ratio conditions specified in the experimental design. Errors in key parameters are modeled as normally distributed variables $\epsilon_x \sim \mathcal{N}(0, \sigma_x)$, where σ_x corresponds to the standard deviation (SD) of the uncertainty associated with parameter x. The assumption of normality is supported by the central limit theorem [40] as well as empirical observations within this study. Accordingly, parameter errors related to the uncertainty model are represented by stochastic parameters $\widetilde{x} = x + \epsilon_x$. Given $K_{\mathrm{p,ideal}}$, the stochastic equilibrium supernatant concentration $\widetilde{c}_{\mathrm{sup}}$ can be evaluated using the following expression derived from Eq. (4):

$$\widetilde{c}_{\mathrm{sup}} = \frac{\widetilde{c}_{\mathrm{L}}}{\frac{\widetilde{V}_{\mathrm{R}}}{\widetilde{V}_{\mathrm{L}}}\left(K_{\mathrm{p,ideal}} + \widetilde{\varepsilon}_{\mathrm{b}}\right) + \frac{\widetilde{V}_{\mathrm{F}}}{\widetilde{V}_{\mathrm{L}}} + 1} + \epsilon_{c_{\mathrm{sup}}} \tag{5}$$

Here, $\widetilde{c}_{\mathrm{L}}$ describes the total perturbed loading concentration, incorporating errors arising from preparation of the protein solution ($\sigma_{c_{\mathrm{L,s}}}$) and concentration measurements ($\sigma_{c_{\mathrm{L,m}}}$). $\epsilon_{c_{\mathrm{sup}}}$ denotes the error in measuring the supernatant concentration. The concentration characterization experiments presented in Fig. 2 show that the SD of the concentration measurement depends on the concentration. Accordingly, the following parameterized function is applied:

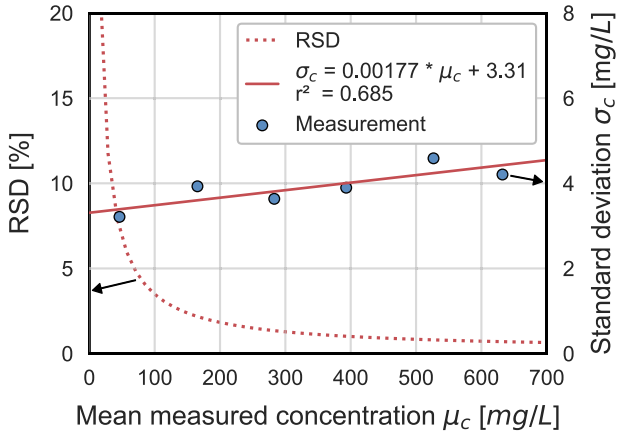

Fig. 2. Trend lines for the absolute (solid) and relative (dotted) standard deviation of protein concentration measurements for six solutions in the relevant HTS range (n = 48 per solution). Black arrows indicate the associated y-axes.

$$\sigma_c = \mathrm{a}_1\, c + \mathrm{a}_2 \tag{6}$$

where a_1 represents the relative contribution and a_2 the absolute contribution to the concentration measurement uncertainty. The total SD of c_{L} is therefore defined as $\sigma_{c_{\mathrm{L}}} = \mathrm{a}_1\, \widetilde{c}_{\mathrm{L,s}} + \mathrm{a}_2$. Finally, the HTS-measured partition coefficient $\widetilde{K}_{\mathrm{p}}$ can be obtained by combining Eqs. (4) and (5), considering the assumed parameter values and the experimental and analytical deviations reflected in $\widetilde{c}_{\mathrm{sup}}$. A detailed derivation of Eq. (7) is provided in the Supplementary Information. For improved readability, the auxiliary quantity A is defined as

$$A = \frac{\widetilde{V}_{\mathrm{R}}}{\widetilde{V}_{\mathrm{L}}}\left(K_{\mathrm{p,ideal}} + \widetilde{\varepsilon}_{\mathrm{b}}\right) + \frac{\widetilde{V}_{\mathrm{F}}}{\widetilde{V}_{\mathrm{L}}} + 1$$

leading to

$$\widetilde{K}_{\mathrm{p}} = \frac{V_{\mathrm{L}}}{V_{\mathrm{R}}}\left(\frac{\widetilde{c}_{\mathrm{L}}}{\frac{\widetilde{c}_{\mathrm{L}}}{A} + \epsilon_{c_{\mathrm{sup}}}} - 1\right) - \frac{V_{\mathrm{F}}}{V_{\mathrm{R}}} - \varepsilon_{\mathrm{b}} \tag{7}$$

Since c_{L} is experimentally determined in each HTS run, its deterministic value is replaced in the uncertainty model by the stochastic parameter $\widetilde{c}_{\mathrm{L}}$, which captures the associated uncertainty. Based on Eq. (7), distributions of $\widetilde{K}_{\mathrm{p}}$ are obtained for a given $K_{\mathrm{p,ideal}}$ using the calibrated parameter distributions and repeated sampling. This approach avoids correlated input variables (e.g., $c_{\mathrm{sup}} = f(K_{\mathrm{p,ideal}}, c_{\mathrm{L}}, V_{\mathrm{L}}, V_{\mathrm{R}}, V_{\mathrm{F}}, \varepsilon_{\mathrm{b}})$) and closely reflects the experimental workflow presented in Fig. 1.

2.3. Monte Carlo uncertainty propagation and parameter contribution analysis

MC sampling propagates uncertainty by replacing analytical probability distributions with large sets of random samples that are propagated through the computational workflow to evaluate the resulting output distribution. This approach is broadly applicable to arbitrary input distributions and nonlinear models. The mathematical foundations and performance characteristics of MC sampling are well documented in the literature [27,41,42]. A typical MC study assigns probability density functions (PDFs) to all input quantities, draws random samples from these distributions, evaluates the model function for each sample, and uses the model outputs to construct a discrete approximation of the output PDF. From this distribution, estimates,

standard uncertainties, and coverage intervals can be derived [27]. MC sampling thus represents a valuable tool in high-throughput experimentation [21,23] as demonstrated by Osberghaus et al. [34]. In this study, stochastic deviations within the experimental procedure were quantified and propagated together with an ideal partition coefficient using MC sampling according to Eq. (7).

Beyond estimating total uncertainty, it is useful to quantify the contribution of individual parameter uncertainties, particularly when establishing or optimizing a new experimental setup or methodology of a HTS workflow. Parameter-specific contributions can be examined through local sensitivity analysis using one-factor-at-a-time (OFAT) sampling. As the OFAT method assumes local linearity, parameter independence, and negligible interaction effects, its suitability must be verified for the specific application [43]. Comparing the resulting parameter-specific variances, either relative to one another or relative to the total variance, enables assessment of the relative influence of each parameter. Similar variance-based analyses are widely used across scientific fields, for example in the uncertainty analysis of Penicillin V production [44] and in environmental studies examining parameter sensitivity and uncertainty in forest carbon flux models [45].

3. Material and methods

3.1. Chromatography resin, buffers, and protein

All chromatography-related experiments were performed using the strong cation exchanger POROS XS (Thermo Fisher Scientific, Waltham, MA, USA). The chemicals used in this study were purchased from Sigma-Aldrich (St. Louis, MO, USA). High-purity water was used for buffer preparation. Ten buffers containing 50 mM sodium acetate (pH 5.0) and 200–290 mM sodium chloride (NaCl) were used for resin equilibration and protein buffer exchange during the HTS experiments. Each buffer was prepared once as a single bulk batch and used consistently throughout all experiments, so that variability in pH and NaCl concentration between wells and plates was minimized and considered negligible for the present workflow. The strip buffer consisted of 50 mM sodium acetate (pH 5.0) and 2 M NaCl. For hold-up volume determination, the equilibration buffer consisted of 50 mM sodium acetate (pH 5.0) and 500 mM sodium nitrate ($NaNO_3$), and the elution buffer consisted of 50 mM sodium acetate (pH 5.0). 20% (v/v) ethanol with 50 mM NaCl was used to adjust the solid-to-liquid ratio of the resin slurry prior to pipetting. A human full-length immunoglobulin G1 (IgG1), provided by Boehringer Ingelheim Pharma GmbH & Co. KG (Biberach, Germany), was used in this study. The antibody was captured through Protein A affinity chromatography, followed by neutralization, sterile filtration through a 0.2 μm filter, and freezing at −70 °C. After thawing, the sample was buffer exchanged into the respective equilibration buffer using a 5 mL HiTrap Desalting column (Cytiva, Marlborough, MA, USA), in accordance with the manufacturer's instructions. The resulting solution was then adjusted with the respective buffer to a concentration of 0.53–0.60 g/L, as quantified using a microplate reader (Tecan Infinite M Nano+; Tecan, Männedorf, Switzerland). Product purity (monomer content > 96.5%) was determined after freeze-thaw by size-exclusion chromatography using an Acquity UPLC Protein BEH SEC column, 200 Å, 4.6 mm x 300 mm (Waters Corporation, Milford, MA, USA).

3.2. Instruments and software

The automated high-throughput workflow and the corresponding characterization experiments were performed on a Tecan Fluent liquid-handling system (Tecan, Männedorf, Switzerland). The station was equipped with two Flexible Channel Arms (FCA) featuring air- and liquid-displacement pipetting, one Robotic Gripper Arm (RGA), two integrated plate shakers (BioShake 3000 elm; QINSTRUMENTS GmbH, Jena, Germany), a microplate reader (Tecan Infinite M Nano+; Tecan, Männedorf, Switzerland), and a plate centrifuge (Rotanta 460 Robotic; Andreas Hettich GmbH & Co. KG, Tuttlingen, Germany). Processes were controlled using FluentControl software (Tecan, Männedorf, Switzerland). For characterization of the pipetted target volume, an analytical balance module (WXS205SDUV; Mettler Toledo, Nänikon, Switzerland) was integrated into the robotic platform. To characterize variations in the distributed dry resin mass, a vacuum centrifuge (Concentrator plus; Eppendorf, Hamburg, Germany) and an analytical balance (Excellence XS64; Mettler Toledo, Nänikon, Switzerland) were used. All data preprocessing, calculations, and visualization were performed using Python 3.12.8 and open-source packages available via the Python Package Index (PyPI). Numerical computations and random number generation for the Monte Carlo sampling were implemented using NumPy (v2.2.2), while data handling was performed using pandas (v2.2.3). Non-linear and linear regression (e.g., power-law and linear fits) was carried out using the curve_fit routine of SciPy (v1.15.2), and normality was assessed using the Shapiro–Wilk test (scipy.stats.shapiro) and quantile–quantile diagnostics (scipy.stats.probplot). Goodness-of-fit metrics (coefficient of determination and root-mean-square error) were computed using scikit-learn (v1.6.1). Figures were generated using Matplotlib (v3.10.0) and seaborn (v0.13.2). For all Monte Carlo simulations, a fixed random seed was used to ensure reproducibility.

3.3. Characterization of experimental error sources

For each experimental error source, dedicated characterization experiments were performed to determine the corresponding parameter distributions under conditions matching the HTS workflow. The normality of these distributions was evaluated using the Shapiro–Wilk test [46], a formal hypothesis test that is particularly powerful for the comparably small sample sizes typical of such characterization experiments, in combination with quantile–quantile (Q-Q) plots [47], which graphically compare the empirical against the theoretical normal quantiles and thereby reveal the nature and location of any deviations. This combination of a formal test and complementary graphical assessment is a widely established method for assessing the normality of experimental data [48,49]. A significance level of $\alpha = 0.05$ was applied throughout.

3.3.1. Protein stock preparation and concentration measurement

To characterize the variability in the load material concentration c_L, two potential sources of error were examined. First, variability arising from preparation of the load protein solution was assessed. The prepared concentration of c_L was intentionally varied across three HTS plates to evaluate contributions to potential plate-to-plate variability. To isolate dilution precision from measurement variability, the concentration c_L at the start of each HTS run was defined as the average of eight measurements. Second, the uncertainty associated with the concentration measurement itself was quantified, as this error source also affects determination of the protein concentration in the supernatant after equilibration with the respective combinations of protein, buffer, and resin. Concentrations were determined by blanked absorbance measurements at 280 nm in UV-transparent microtiter plates (96 well UV-STAR, Greiner Bio-One, Kremsmünster, Austria), with optical pathlength corrections based on absorbance measurements at 900 and 977 nm, following McGown and Hafeman [50]. Six evenly spaced concentrations within the relevant HTS range were prepared and measured in 16 replicates on three plates, yielding 48 measurements per concentration level and enabling analysis of the SD as a function of concentration.

3.3.2. Liquid pipetting

To characterize the variability in the pipetted load volume, V_L, high-purity water with a target volume of 200 μL was pipetted using an air-displacement LiHA equipped with 1000 μL disposable tips (DiTi) into a reservoir placed on the integrated analytical balance module. Assuming a constant density for high-purity water of 0.9982 g/cm^3, 30 pipetting repetitions followed by weight determination enabled

estimation of the pipetted load volume distribution.

3.3.3. Resin slurry dispensing

To characterize the variability in the pipetted chromatography resin volume, V_R, a 25% (v/v) slurry of POROS XS was prepared by settling the resin overnight. Five mL of the resuspended slurry was pipetted manually into a 24 deep-well plate (Riplate SW, Avantor, Radnor, PA, USA) placed on the orbital shaker operating at 450 rpm. After a pipette-mixing sequence, the target slurry volume of 100 µL was aspirated from the continuously agitated deep-well plate and dispensed into pre-weighed 1.5 mL Eppendorf tubes using an optimized liquid handling protocol for resin slurry aspiration and dispensing on the air-displacement LiHA equipped with pre-wetted 1000 µL DiTis. Subsequently, the tubes were centrifuged under vacuum at 30 °C for 12 h to remove residual liquid and were then weighed again. Assuming constant density of the dried resin, relative variations in the measured resin mass directly reflect relative variations in the dispensed resin volume. Therefore, 30 pipetting repetitions and the corresponding weight measurements were used to estimate the distribution of dispensed resin volumes around the target value of 25 µL.

3.3.4. Hold-up correction

To characterize the variability in the hold-up volume associated with the filter plate frit (V_F) and the batch hold-up porosity (ε_b), hold-up volumes were determined in a dedicated characterization experiment for five different resin quantities ranging from 0 to 50 µL. The tracer $NaNO_3$ was used specifically for this hold-up characterization, whereas all subsequent K_p experiments employed the NaCl-containing buffer system described above. Resin slurry was distributed to the 96-well filter plate (Multiscreen PVDF, Merck, Darmstadt, Germany) according to the procedure described in Section 3.3.3. Initially, the ethanol storage solution was removed by centrifugation of the filter plate stacked on a microtiter plate for 30 s at 1500 rpm. Buffer equilibration of the resin was performed in three cycles, each consisting of dispensing 200 µL of $NaNO_3$ equilibration buffer to each well, orbital shaking at 1100 rpm for 20 min, and subsequent evacuation by centrifugation as described in the previous step. This equilibration and centrifugation cycle was kept constant throughout the experiment and the standard HTS workflow shown in Fig. 1. The $NaNO_3$ concentration in the supernatant of the third cycle was measured at 302 nm, with optical path-length corrections based on absorbance readings at 900 and 977 nm. Next, 200 µL of elution buffer was dispensed, equilibrated, and evacuated, followed by measurement of the final $NaNO_3$ concentration. A mass balance over each well was used to calculate the corresponding hold-up volume. Each resin volume was tested 16 times on three plates, yielding 48 measurements per resin volume level. The distribution of V_F was estimated from wells containing no added resin, while the distribution of ε_b was determined by linear regression of hold-up volume against pipetted resin volume.

3.4. Automated filter-plate-based high-throughput screening

The HTS workflow, as illustrated in Fig. 1, began with the distribution of 25% (v/v) POROS XS slurry into the filter plate to a target volume V_R of 25 µL, as described in Section 3.3.3. Ethanol storage solution in each well was removed by centrifugation, followed by three cycles of equilibration with buffers containing the respective NaCl concentrations. All orbital shaking and evacuation cycles throughout the workflow were carried out according to the procedure described in Section 3.3.4. The evacuated buffer from the third equilibration cycle was used as a blank. Before loading each well, the protein concentration was measured, according to the method given in Section 3.3.1. The targeted load concentrations for the three repetitions of the workflow were approximately 562.5 mg/L and intentionally varied between the runs. Subsequently, 200 µL of the protein solution was dispensed into each well, followed by 20 min of orbital shaking at 1100 rpm without plate cover, evacuation, and concentration measurement of the supernatant. The incubation time of 20 min was selected based on preliminary adsorption kinetic studies, which confirmed that equilibrium was reached well within this period under the applied conditions (Supplementary S1). These measurements enabled calculation of K_p using Eq. (4). Finally, two equilibration cycles with high-salt strip buffer were performed to remove any bound protein from the resin, thereby enabling closure of the total mass balance. The entire workflow was repeated three times with freshly prepared filter plates and protein stock solutions.

3.5. Monte Carlo simulation and analysis framework

3.5.1. Simulation algorithm

The simulation algorithm propagates the stochastic parameters through the uncertainty model described in Section 2. These calculations were performed across the full range of relevant $K_{p,ideal}$ values (0–100) that span the transition between binding and non-binding process regimes. For a given $K_{p,ideal}$, normally distributed random samples were generated for all relevant experimental parameters using the mean and standard deviation obtained from the characterization experiments. These sampled inputs were inserted into Eq. (7) to compute simulated $\widetilde{K}_p$ values. Each simulation consisted of 10,000 independent samples to ensure stable estimation of distributional properties, with convergence verified by assessing the predicted standard deviation as a function of sample size.

3.5.2. Model validation

To validate the uncertainty model, the HTS workflow (Fig. 1) was applied in a case study involving a mAb monomer, POROS XS, and 10 buffers with constant pH and increasing NaCl concentrations (c_{NaCl}) spanning the transition from binding to non-binding conditions. For each condition, 24 replicates were measured across three independently prepared plates. The model was validated by testing whether the experimentally observed spread across the purification-relevant $K_{p,ideal}$ range can be reproduced by the uncertainty model when supplied with the experimentally characterized parameter distributions. Assuming approximately normally distributed measurement variability, $K_{p,ideal}$ was defined as the mean of the corresponding experimental measurements. The dependence of $K_{p,ideal}$ on c_{NaCl} was modeled using a power-law fit, $K_{p,ideal} = b_1\, c_{NaCl}{}^{b_2}$. This selection is justified by the SMA model, which exhibits an analogous power-law functional form under linear-isotherm conditions [51]. The simulation algorithm described above was used to predict the variability of $\widetilde{K}_p$ over the full c_{NaCl} range. Model validity was assessed by comparing the model-derived 95% confidence interval (CI_{95}) with the experimentally observed variability, complemented by a quantitative comparison of the predicted and measured SD of $\widetilde{K}_p$.

3.5.3. Parameter contributions to uncertainty and phase ratio perturbation

The contribution of each experimental error to the total measurement uncertainty was evaluated by analysis of the variance contributions of the associated parameters. Using OFAT sensitivity analysis, each parameter was sampled independently within its characterized distribution, while all other parameters were fixed at their mean. The ratio of the variance of $\widetilde{K}_p$ induced by variation of a single parameter to the total variance obtained by simultaneously varying all parameters yields the relative contribution of each experimental error. This computationally efficient approach is valid under the assumption of parameter independence and negligible interaction effects. The adequacy of this approach was assessed by evaluating the residual variance between the total variance and the sum of the single-parameter variances.

To further assess sensitivity to changes in parameter uncertainty, the SDs of the parameter distributions were systematically scaled and

propagated through the same simulation framework. The SD of the investigated parameter was perturbed by ±10%, ±25%, and ±50%.

Finally, the influence of experimental design on the $\widetilde{K}_p$ distribution was assessed by perturbing the phase ratio $\beta = V_L/V_R$. Assuming a constant resin loading of 5 g/L, a fixed working volume per well given by $V_W = V_L + V_R = 225\ \mu L$, and constant relative standard deviations (RSDs) for all parameters across the investigated β range, the impact of varying phase ratios (1–50) across the full range of $K_{p,ideal}$ was evaluated. The resulting simulation outputs, including the corresponding protein demand per 96-well plate for each β, were visualized in a single response-surface representation (Fig. 7).

4. Results and discussion

4.1. Characterization of experimental errors

To characterize uncertainty in all model parameters and evaluate the assumption of normality, the distributions of the following quantities were experimentally determined: the prepared loading protein concentration $\widetilde{c}_{L,s}$, the dispensed load volume $\widetilde{V}_L$, the resin volume $\widetilde{V}_R$, the batch hold-up porosity $\widetilde{\varepsilon}_b$, and the filter-plate frit-derived hold-up volume $\widetilde{V}_F$. In addition, the precision of concentration measurements ($\widetilde{c}_{sup}$ & $\widetilde{c}_{L,m}$) across the relevant analytical range was assessed. All calibration experiments were performed under conditions matching those of the HTS workflow shown in Fig. 1, with a target replicate number of at least 30 found to be sufficient for a robust estimation of the parameter distributions. The only exception was $\widetilde{c}_{L,s}$, which was based on three intentionally and widely varied stock solutions across the three plate runs. The experimental results are summarized in Table 1. Because the dominant uncertainty contributors are workflow- and equipment-specific rather than protein-specific, the calibration experiments only need to be performed once and can subsequently be applied to other proteins under the same assay conditions on the same equipment.

4.1.1. Concentration measurement

Within the applied HTS workflow, protein concentrations were measured both in the loading solution and in the evacuated supernatant after equilibrium was established. Consequently, measurement precision had to be evaluated across the full concentration range from 0 mg/L to c_L. Fig. 2 shows the standard deviations (σ_c) of the six mean concentration levels (μ_c; n = 48 per concentration), the corresponding linear regression, and the resulting RSD curve. The data exhibited a linear trend in σ_c with a coefficient of determination ($r^2 = 0.685$), a slope of 0.00177, and an intercept of 3.31 mg/L. This behavior is expected, as the uncertainty of absorbance measurements is known to increase approximately proportionally with the absorbance value, which itself scales linearly with protein concentration under the Beer-Lambert law [52]. For simplicity, the uncertainty analysis in this study focuses on concentration-based errors. Alternatively, the error can also be expressed in terms of absorbance, which allows a more direct comparison across different proteins. The asymmetry in relative uncertainty is reflected in the RSD profile: RSD values remain below 2% for concentrations above 186 mg/L but increase exponentially at lower concentrations, reaching 25.1% at 13 mg/L, consistent with previous findings [53]. In terms of $\widetilde{K}_p$, this implies that the contribution of uncertainty in the concentration measurement to the overall $\widetilde{K}_p$ uncertainty behaves inversely, being relatively small at low $K_{p,ideal}$ values and increasing exponentially at high $K_{p,ideal}$.

The normality of concentration measurement errors was assessed using Q-Q plots and Shapiro-Wilk tests for each protein concentration. A representative result is shown in Supplementary S2(a), with a full overview for all six concentrations in Supplementary S3. Overall, statistical tests, diagnostic plots, and small residual deviations provide strong evidence for approximate normality across five of six concentrations.

Table 1
Summary of the parameter-characterization results. Each distribution of n repeats is described by its mean (μ), standard deviation (σ), and relative standard deviation (*RSD*).

	$\widetilde{c}_{sup}$ & $\widetilde{c}_{L,m}$ [mg/L]	$\widetilde{c}_{L,s}$ [mg/L]	$\widetilde{V}_L$ [µL]	$\widetilde{V}_R$ [µL]	$\widetilde{\varepsilon}_b$ [−]	$\widetilde{V}_F$ [µL]
µ	–	569.9	199.0	25.0	0.748	3.50
σ	$0.00177 * \mu + 3.31$	26.33	2.31	1.10	0.0278	0.442
RSD [%]	$0.177 + \frac{331}{\mu}$	4.62	1.16	4.38	3.72	12.6
n	48	3	30	30	48	48

4.1.2. Protein stock preparation

For reliable determination of K_p, operation in the linear region of the adsorption isotherm must be ensured. In this study, POROS XS was operated at loadings below 5 g/L of resin, which exhibited linear behavior in preliminary isotherm experiments (data not shown). Under these conditions, variations in c_L do not influence protein partitioning [51]. Differences in the measurement uncertainty of $\widetilde{c}_{sup}$ resulting from variability in $\widetilde{c}_{L,s}$ are expected to be negligible. At a fixed $K_{p,ideal}$, changes in $\widetilde{c}_{L,s}$ propagate to $\widetilde{c}_{sup}$ and its associated uncertainty $\sigma_{c_{sup}} = f(\widetilde{c}_{sup}(\widetilde{c}_{L,s}, K_{p,ideal}))$. However, the resulting fluctuations in $\widetilde{c}_{sup}$ are very small and thus have only a marginal effect on $\sigma_{c_{sup}}$. Nevertheless, this effect is explicitly included in the uncertainty model. Protein stock solutions were prepared individually for the three validation plates with concentrations corresponding to loadings between 4.27–4.73 g/L of resin, enabling assessment of their influence on the experimental outcome. To incorporate $\widetilde{c}_{L,s}$ variability into the uncertainty model, the mean concentration of 569 mg/L with a corresponding RSD of 4.62% (26.33 mg/L) was used. No extensive testing of normality was conducted for this parameter, as the intentionally exaggerated variation serves to confirm that $\widetilde{c}_{L,s}$ fluctuations do not significantly affect the outcome of the HTS.

4.1.3. Liquid pipetting

Pipetting of the loading volume $\widetilde{V}_L$ is another key parameter that requires characterization. The distribution of $\widetilde{V}_L$ is shown in Supplementary S2(b) (n = 30) and yields an average dispensed volume of 199.0 µL with a SD of 2.31 µL (Table 1). Normality was confirmed based on graphical diagnostics and the Shapiro-Wilk test. The resulting RSD of 1.16% closely matches the RSDs reported by Osberghaus et al. for protein (1.3%) and buffer solutions (1.5%) [34], supporting the choice of water as a practical surrogate for the representative HTS workflow investigated here. While liquid-class settings and liquid properties may influence pipetting performance [50], these effects were not investigated separately. As the buffers used here span only a moderate salt range (200–290 mM NaCl) and the load material was characterized under representative conditions, concentration-dependent variations in liquid properties were not expected to contribute substantially. Such effects can nevertheless be incorporated into the framework through workflow-specific characterization if required.

4.1.4. Resin slurry dispensing

A key topic in the literature on filter-plate-based HTS of K_p is the precise definition of the resin volume V_R, with multiple strategies available for preparing plates [16,19,22,54]. In this study, we employed overnight sedimentation to obtain a 25% (v/v) slurry concentration, followed by LHS pipetting under orbital shaking. This approach requires no specialized equipment and offers high flexibility with respect to different chromatography resins and quantities. To quantify the SD of $\widetilde{V}_R$ around the defined volume (25 µL), the pipetted slurry samples were centrifuged under vacuum to remove all liquid, and the dry weight of each sample was determined using an analytical balance (n = 30).

Because the resin density can be assumed constant across samples, the RSD of the measured masses directly reflects the RSD of the corresponding volumes and is independent of how the volume is defined. As summarized in Table 1, the resulting RSD was 4.38% (1.095 µL), and both graphical diagnostics and the Shapiro-Wilk test indicate normality (Supplementary S2(c)).

4.1.5. Hold-up correction

The final parameters of the uncertainty model, $\widetilde{V}_F$ and $\widetilde{\varepsilon}_b$, define the hold-up volume correction, which reflects dilution of the protein load by residual equilibration buffer remaining from resin conditioning in the filter-plate-based HTS workflow. The linear trend obtained with the $NaNO_3$-based assay by Ram et al. [39] was successfully reproduced in our characterization experiments (Fig. 3). In line with these observations, V_H is expressed as the sum of a filter-derived volume V_F and a term scaling with resin volume V_R via the batch hold-up porosity ε_b. This formulation isolates the V_R-dependent contribution and enables resin-specific hold-up volume quantification. The distribution of $\widetilde{V}_F$ (μ_{V_F} = 3.50 µL, σ_{V_F} = 0.442 µL) was obtained from measurements without added resin, whereas the distribution of $\widetilde{\varepsilon}_b$ (μ_{ε_b} = 0.748, σ_{ε_b} = 0.0278) was determined by linear regression of the full dataset. Each value is based on n = 48 replicates to ensure robust estimation of the parameter distribution.

As shown in Supplementary S2(d), $\widetilde{V}_F$ exhibits excellent agreement with a normal distribution, supported by both the Shapiro-Wilk test and graphical diagnostics. The assumption of normally distributed measurement data of $\widetilde{V}_H$ across varying resin volumes is justified, as these measurements are strongly influenced by $\widetilde{V}_F$ and $\widetilde{V}_R$. Consequently, the estimated slope $\widetilde{\varepsilon}_b$ is likewise expected to follow a normal distribution, since it forms a linear combination of normally distributed variables. Because variations in V_R systematically propagate into the measured V_H, this relationship can conversely be exploited to estimate relative resin volumes non-invasively. Accordingly, the $NaNO_3$ assay also offers a simple and rapid method to compare resin volumes across wells in filter-plate-based HTS formats.

4.2. Uncertainty model validation

Model validation was performed in a case study using a mAb monomer and POROS XS resin, tested at 10 increasing NaCl concentrations spanning the transition from binding to non-binding regimes. For each condition, 24 replicates were conducted on three independently prepared plates following the HTS routine shown in Fig. 1, which provided a robust basis for validating the predicted variability. Model validity was defined as the ability to reproduce the observed spread in $\widetilde{K}_p$ based on the characterized parameter uncertainties, with the mean of each measurement series expected to match $K_{p,ideal}$. The precision of these means was confirmed by the relative standard error, i.e. the Type-A standard uncertainty of the mean ($\sigma/\sqrt{n}$; [27]) expressed relative to the mean, which ranged from 1.2% to 3.8% across all conditions and thus indicates a reliable estimation of $K_{p,ideal}$.

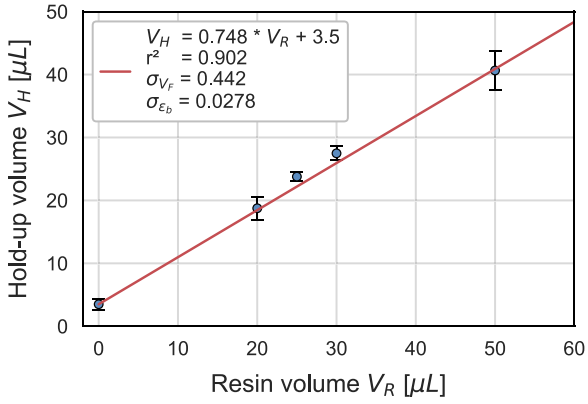

Fig. 3. Trend line for hold-up volume measurements (n = 48 per resin volume) across five pipetted POROS XS resin volumes, obtained in the characterization experiment using $NaNO_3$ as a tracer. The intercept and slope correspond to the mean hold-up filter volume μ_{V_F} and mean batch hold-up porosity μ_{ε_b}, respectively. Associated standard deviations are σ_{V_F} and σ_{ε_b}.

All experimental data was captured successfully, with an average mass balance of ≈ 97% after the strip steps. As pronounced evaporation would be expected to concentrate the supernatant and thereby inflate the apparent recovery beyond 100%, the near-complete closure obtained here indicates that evaporation did not contribute substantially under the applied conditions. The experimental and model-derived $\widetilde{K}_p$ distributions are summarized in Table 2, displaying heteroscedastic behavior. Lower c_{NaCl} values, corresponding to higher $K_{p,ideal}$ values in CEX, exhibit higher absolute SD. Across the K_p range between 3 and 100 ($c_{NaCl} \leq 260$ mM), the experimental RSD remains below 10%, while it increases slightly for the remaining conditions down to $K_p = 0.48$, but stays below 20%. Notably, this level of precision indicates that uncertainty is small relative to the separation between the operational regimes. Toward low K_p, the absolute standard deviation of $\widetilde{K}_p$ decreases continuously, while only the relative uncertainty increases, so that the absolute measurement uncertainty becomes very small in this region. Consequently, the screening workflow can robustly discriminate between distinct operational regimes, including bind-and-elute behavior ($K_p \geq 100$) and weak partitioning ($K_p \approx 0.1$–20). Although the investigated conditions do not extend into the true flowthrough regime ($K_p < 0.1$), the lowest observed partition coefficient of $K_p = 0.48$ already lies within the onset of the non-binding regime, and the favorable absolute-uncertainty trend toward low K_p indicates that such conditions can be reliably distinguished from weak partitioning regime [36]. The high precision observed across these regimes indicates excellent repeatability of this filter-plate-based HTS workflow and provides a reliable quantitative basis for describing resin adsorption behavior, justifying the wide application of comparable HTS workflows in process development.

Fig. 4 displays the experimental $\widetilde{K}_p$ values determined on three individual plates. A power-law function was fitted to the mean values of each condition ($r^2 = 0.999$), providing a continuous trajectory of $K_{p,ideal}$ across the investigated c_{NaCl} range. Based on the fitted trajectory of $K_{p,ideal}$, CI_{95} was calculated and is shown as the surrounding shaded region. The calibrated uncertainty model captures the experimental variability observed in the data. The pronounced heteroscedastic trend is accurately reproduced. Although the model underestimates the experimental SD by up to ≈ 22% at 210 mM and 270 mM, the agreement between modeled and observed uncertainty remains strong, particularly given the inherent complexity of HTS workflows. These findings provide strong confidence that the established modeling framework reliably captures the dominant contributors to experimental variability in the filter-plate-based HTS. Consequently, the framework enables uncertainty quantification even when only single replicates are available, and supports the definition of objective acceptance criteria for conditions evaluated in duplicate. As discussed above, additional characterization experiments are only required following workflow- or equipment-specific changes to the presented HTS, rendering this approach readily transferable and enabling systematic identification of the primary uncertainty drivers.

Additionally, the distribution characteristics of the experimental and model-derived results, as well as the plate-to-plate variability, were analyzed in more detail. Fig. 5 shows histograms of the $\widetilde{K}_p$ values for each plate, together with kernel density estimates (KDEs) of the combined plates and modeled data across all c_{NaCl} conditions. The model output appears approximately normal based on graphical diagnostics, and Shapiro–Wilk tests do not reject normality for the experimental data in 8 of 10 cases. Together, these results support estimating the $K_{p,ideal}$

Table 2
Overview experimental and model-derived $\widetilde{K}_p$ distributions.

[mM]	200	210	220	230	240	250	260	270	280	290
$\widetilde{K}_p = K_{p,ideal}$ [-]	90.98	49.40	25.85	13.10	7.16	3.96	2.29	1.35	0.80	0.48
σ_{exp} [-]	7.931	4.461	1.52	0.828	0.514	0.228	0.181	0.175	0.097	0.0875
σ_{model} [-]	8.778	3.47	1.53	0.737	0.417	0.257	0.178	0.137	0.114	0.098
RSD_{exp} [%]	8.72	9.03	5.88	6.32	7.18	5.76	7.90	12.98	12.14	18.42
RSD_{model} [%]	9.65	7.02	5.92	5.63	5.82	6.50	7.77	10.16	14.27	20.63

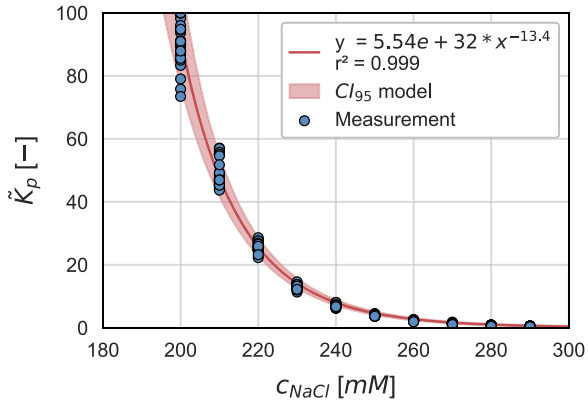

Fig. 4. Validation of model uncertainty. Experimental $\widetilde{K}_p$ values from the case study (n = 24 per solution) showing the spread of the measured partition coefficient across 10 NaCl concentrations (c_{NaCl}). The mean $\widetilde{K}_p$ is fitted with an exponential function to represent the trajectory of $K_{p,ideal}$; the shaded band denotes the model-derived 95% confidence interval.

trajectory from experimental means under the assumption of normality. Regarding plate-to-plate variability, small plate-specific shifts are visible under identical conditions, with the second plate generally showing higher values. However, the distributions overlap strongly and fall well within the model-predicted variability. Therefore, the observed plate-to-plate variability can be attributed to the modeled parameter variability and motivates further investigation of the underlying error sources in the following section.

Lastly, sufficient convergence of the MC sampling was assessed by monitoring the SD of $\widetilde{K}_p$ and the relative residuals as a function of sample size, using the maximum sample size as a reference. As shown in Supplementary S4, the SD and relative residuals stabilized at approximately 5000 samples, indicating robust convergence of the MC estimates (10,000 samples) and further supporting the reliability of the generated results. The customary log transformation of $\widetilde{K}_p$ values and the resulting linearization were omitted in this study to preserve the heteroscedastic trend and to facilitate identification of individual parameter contributions.

4.3. Dominant experimental error sources contributing to uncertainty

The absolute and relative contributions of individual parameters to the uncertainty in $\widetilde{K}_p$ within the presented workflow were quantified using an OFAT sensitivity analysis. This approach enables identification of the dominant sources of uncertainty, providing insight into the propagation of experimental errors and improving confidence in the HTS-derived data. The validity of the OFAT approach relies on the assumption of parameter independence and negligible interaction effects, supported by the close agreement between the total variance and the sum of the single-parameter variances (± 2% across most of the $K_{p,ideal}$ range; Supplementary S5). To connect the variance decomposition to actionable experimental refinement, we further performed perturbation analyses in which the SD of each parameter was systematically varied, evaluating how changes in experimental precision translate into changes in the uncertainty of $\widetilde{K}_p$ (Supplementary S6). This enables risk-based method optimization, which is demonstrated for the present HTS workflow.

Fig. 6 summarizes the results, with subpanel (a) showing the SD of $\widetilde{K}_p$ induced by individual parameters and subpanel (b) presenting the corresponding relative variance contributions of the individual error sources as a percentage of the total variance. This representation was chosen because SD conveys the absolute magnitude of uncertainty in $\widetilde{K}_p$, whereas variance enables decomposition into parameter contributions consistent with established variance-based sensitivity analysis methods [43]. As reflected by the trend of the SD in $\widetilde{K}_p$, the total uncertainty exhibits heteroscedastic behavior. This behavior follows directly from Eq. (7): although the parameter variances are constant, their contributions scale with $K_{p,ideal}$, leading to an increase in the propagated variance of $\widetilde{K}_p$.

Two experimental error sources dominate the uncertainty across nearly the entire range of $K_{p,ideal}$: (i) uncertainty in the dispensed resin volume $\widetilde{V}_R$ and (ii) uncertainty in the measured supernatant concentration $\widetilde{c}_{sup}$. Together, these sources account for > 97% of the total variance across most conditions in the investigated $K_{p,ideal}$ range (Supplementary S5). Variability in $\widetilde{V}_R$ causes a linear rise in the SD of $\widetilde{K}_p$ with increasing $K_{p,ideal}$, as a larger fraction of the equilibrium uptake is inferred from the mass balance. In contrast, variability in $\widetilde{c}_{sup}$ leads to an exponential increase in the SD of $\widetilde{K}_p$ across $K_{p,ideal}$. This behavior arises because $\widetilde{c}_{sup}$ decreases with rising $K_{p,ideal}$ and, consequently, the relative uncertainty of low-concentration measurements increases sharply as shown in Fig. 2. These findings provide a physical explanation of the observed heteroscedasticity and are in line with the hypothetical effects described by Bergander and Lacki [18].

Based on these findings, resin slurry preparation and dispensing, together with plate-specific biases in UV-based concentration measurements, emerge as the primary drivers of plate-to-plate variability. This interpretation is consistent with reported challenges associated with self-prepared filter-plates [22,54] and with known microplate-specific optical and geometric effects, as well as the intrinsic susceptibility of UV absorbance measurements to systematic inter-plate variability [55,56]. In addition, operator-to-operator differences during HTS execution may contribute to plate-level offsets, but are not explicitly captured in the current model.

Importantly, the presented framework not only identifies these two dominant error sources but also places them in relation to other error sources and quantifies how their relative contributions evolve with $K_{p,ideal}$. The variance contributions of $\widetilde{V}_R$ and $\widetilde{c}_{sup}$ exhibit symmetric, opposing trends and intersect twice, thereby delineating distinct dominance regimes. $\widetilde{c}_{sup}$ dominates at very low $K_{p,ideal}$ (< 1.44), where the mobile phase concentration governs the measurement, and again at higher $K_{p,ideal}$ (>38.26), where $\widetilde{c}_{sup}$ approaches the lower limit of quantification and measurement RSD increases markedly. $\widetilde{V}_R$ dominates in the intermediate regime, where the stationary phase becomes increasingly important, while concentrations remain sufficiently above the quantification limit for concentration measurements. Consequently, this regime-dependent dominance provides a rational basis for

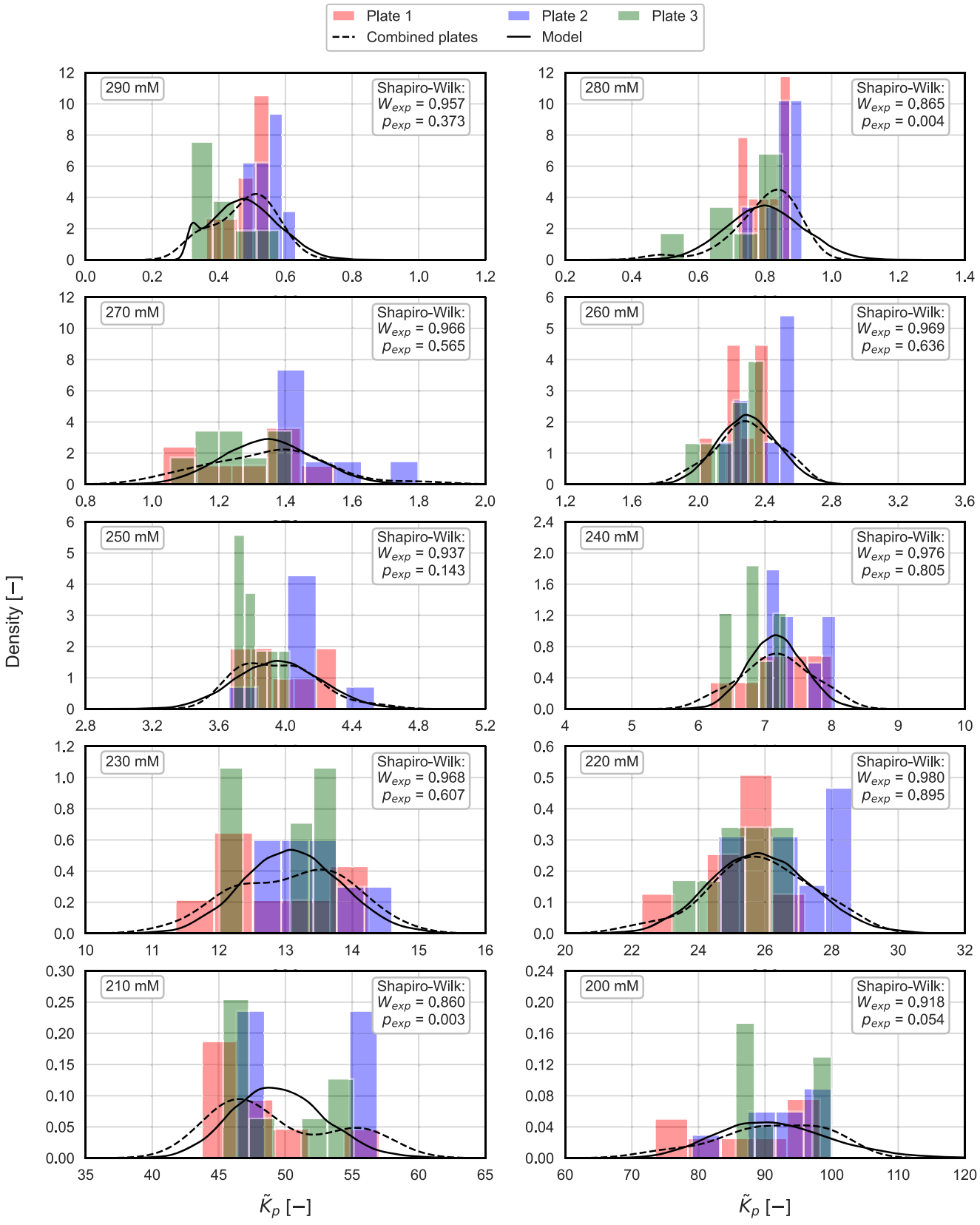

Fig. 5. Histograms of the experimental $\tilde{K}_p$ measurements from the three individual plates (n = 8 per solution per plate) are shown for all 10 NaCl concentrations. Each panel overlays the KDE of the combined experimental dataset (dashed; n = 24) and the corresponding model prediction (solid). Shapiro-Wilk test results (W, p) are reported for each combined experimental distribution.

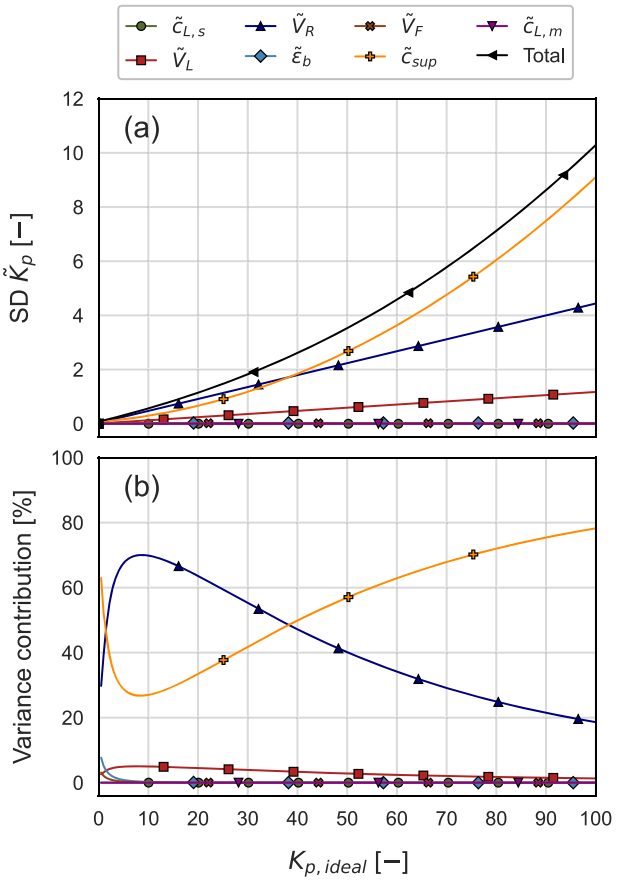

Fig. 6. Parameter contributions to uncertainty in the partition coefficient $\widetilde{K}_p$ as a function of the ideal partition coefficient $K_{p,ideal}$. (a) Standard deviation of $\widetilde{K}_p$ obtained from Monte Carlo OFAT simulations (one parameter perturbed at a time; n = 10,000) and from the total uncertainty model (all parameters perturbed; n = 10,000). (b) Relative variance contributions of each parameter reported as a percentage of the total variance ($100\% * \boldsymbol{Var_i}/\boldsymbol{Var_{total}}$).

prioritizing optimization efforts toward the experimentally most relevant $K_{p,ideal}$ range.

Although the workflow already provides high precision, perturbation analyses of the experimentally estimated SD indicate that optimization of slurry dispensing and supernatant concentration measurement can still substantially improve overall precision across the full $K_{p,ideal}$ range (Supplementary S6(c)). Such analyses are particularly valuable for less optimized HTS setups, as they enable targeted method optimization. To improve precision in resin handling, published strategies such as generation of equally sized particle plugs, gravimetric calibration of slurry dispensing, and in-line resin quantification can be evaluated within the model framework established here [19–21]. With respect to $\widetilde{c}_{sup}$, the perturbation analysis (Supplementary S6(f)–(g)) identifies the absolute error term a_2 as the primary lever. Varying a_2 has a substantially larger effect on both the SD and variance contribution to $\widetilde{K}_p$ than comparable changes in the relative term a_1. This effect is most pronounced at high $K_{p,ideal}$, where $\widetilde{c}_{sup}$ is low and measurement uncertainty drives error propagation. Consequently, the most effective routes to improved $\widetilde{K}_p$ precision are lowering the effective limit of quantification or, if further instrumentation or method optimization is not feasible, increasing $\widetilde{c}_{sup}$ through phase-ratio and/or loading adjustments, as discussed in the next section.

Among the other investigated input parameters, the load volume $\widetilde{V}_L$ is the only parameter that contributes significantly to the variability of $\widetilde{K}_p$ across the full range of $K_{p,ideal}$. Its absolute contribution increases linearly with $K_{p,ideal}$, analogous to the behavior observed for $\widetilde{V}_R$. This shared behavior follows from Eq. (4), which shows that the inverse phase ratio ($V_R/V_L = 1/\beta$) scales the propagated uncertainty in $\widetilde{K}_p$ linearly. Accordingly, accurate establishment of the phase ratio is critical for reliable calculation of the stationary phase concentration and therefore for accurate determination of K_p, consistent with the literature [18,51]. The perturbation analysis further demonstrates that the SD of $\widetilde{K}_p$ induced by uncertainties in $\widetilde{V}_L$ and $\widetilde{V}_R$ scales linearly with the respective parameter uncertainty (Supplementary S6(b)–(c)); thus, halving the parameter SD results in a proportional reduction in the SD of $\widetilde{K}_p$. This linear relationship provides an effective lever for experimental optimization. Given the already high precision of the liquid-handling step (RSD = 1.16%), further improvements should preferentially target the precision of resin distribution as discussed above (RSD = 4.38%).

The remaining parameters fall into two categories. First, the batch hold-up porosity $\widetilde{\varepsilon}_b$ and the liquid hold-up volume associated with the filter-plate frit $\widetilde{V}_F$, which both contribute constant absolute values to the SD of $\widetilde{K}_p$ (0.028 and 0.018, respectively). As shown by Eq. (4), both parameters enter the expression as additive correction terms independent of the equilibrium partitioning, and consequently their contributions do not scale with increasing $K_{p,ideal}$. Physically, both parameters represent the hold-up correction term V_H, which dilutes the mobile phase concentration. Their influence is therefore most pronounced at low K_p and high c_{sup}, where dilution effects have the largest absolute impact [16]. Nevertheless, their relative contribution to the overall uncertainty of $\widetilde{K}_p$ remains limited to 7.67% ($\widetilde{\varepsilon}_b$) and 3.10% ($\widetilde{V}_F$). Accordingly, the proposed determination of hold-up volumes is sufficiently robust, and their associated uncertainty can be regarded as negligible.

Second, uncertainties in the prepared protein loading solution $\widetilde{c}_{L,s}$ and its analytical determination $\widetilde{c}_{L,m}$ were evaluated. Although both parameters exhibit a linear dependence on $K_{p,ideal}$, their contributions to the overall uncertainty remain negligible. This outcome is a direct consequence of operation within the linear regime of the adsorption isotherm, which is inherently reflected in the model structure, since equilibrium partitioning is independent of protein concentration.

For the filter-plate-based HTS workflow presented here, all dominant sources of experimental uncertainty were experimentally characterized, propagated, and validated on a Tecan Fluent LHS, with no further error contributions required to reproduce the observed variability. Beyond this specific workflow, the framework is not limited to the error sources investigated in this study. Workflow- or equipment-specific factors that may become relevant for other assay configurations, such as conditions used during evacuation of the supernatant (e.g., centrifugation speed, centrifugation time, or vacuum level), alternative resin dispensing strategies, resin-specific properties, modifications of analytical procedures, uncertainties from buffer preparation (pH, NaCl concentration), or evaporation effects, can be readily incorporated through experimental characterization of the corresponding parameter distributions and subsequent uncertainty propagation. As these factors were either kept constant or rendered negligible in the present workflow, their assessment was not required here and was intentionally left outside the scope of this study. The framework nevertheless provides a general basis for evaluating the impact of such variations whenever they become relevant. Accordingly, different liquid-handling systems and their respective calibration states may yield different SD or RSD values and therefore need to be characterized independently.

4.4. Effect of phase ratio on the trade-off between precision and protein demand

Adjustments to the experimental design, particularly through changes in the phase ratio ($\beta = V_L/V_R$), provide an effective lever to

modulate the overall uncertainty of K_p measurements by systematically altering the underlying parameter values that drive uncertainty propagation. In contrast to heuristic phase ratio selection, the proposed uncertainty model enables a quantitative assessment of how β influences both the attainable precision of $\widetilde{K}_p$ and the associated protein demand per 96-well plate. This analysis is performed under constant resin loading (5 g/L resin), fixed working volume V_W (225 µL), and experimentally observed constant RSDs, as illustrated in Fig. 7. The framework thus demonstrates its ability to compare alternative experimental designs and to guide the rational selection of β values that balance material constraints and precision requirements of the intended HTS application.

The calculated response surface reveals a consistent trend: decreasing β leads to a pronounced reduction in the SD of $\widetilde{K}_p$ across the entire $K_{p,ideal}$ range. At constant loading and V_w, lowering β increases the effective resin volume while reducing the liquid volume. This shift raises the equilibrium supernatant concentration $\widetilde{c}_{sup}$ at a given $K_{p,ideal}$. The uncertainty in $\widetilde{c}_{sup}$ plays a dominant role in $\widetilde{K}_p$ variability. As shown previously, the RSD of concentration measurements increases exponentially at low analyte levels. Consequently, the increase in $\widetilde{c}_{sup}$ leads to a significant reduction in the uncertainty of $\widetilde{K}_p$, particularly at high $K_{p,ideal}$.

In contrast, uncertainties in $\widetilde{V}_R$ and $\widetilde{V}_L$ do not introduce an intrinsic β-dependence in the SD of $\widetilde{K}_p$. According to Eq. (7), their contribution arises primarily through the ratio $\widetilde{V}_R/\widetilde{V}_L$, which scales the propagated uncertainty with $K_{p,ideal}$. To make this relationship transparent, Gaussian error propagation is applied here as a complementary closed-form check and yields

$$\sigma_{\widetilde{V}_R/\widetilde{V}_L} = 1/\widetilde{\beta}\ \sqrt{RSD^2_{\widetilde{V}_R} + RSD^2_{\widetilde{V}_L}}$$

This expression shows that the β-dependence of the SD of the phase ratio is negligible, as the RSDs of $\widetilde{V}_L$ and $\widetilde{V}_R$ are small and constant. Consequently, the SD of $\widetilde{V}_R/\widetilde{V}_L$ remains approximately invariant with respect to β. Since the remaining input parameters contribute only marginally to the overall variance, the observed trend in the SD of $\widetilde{K}_p$ is dominated by β-dependent changes in the supernatant concentration and the associated measurement precision.

A potential limitation of the present analysis is that β-dependent changes in the RSD of $\widetilde{V}_L$, $\widetilde{V}_R$, $\widetilde{\varepsilon}_b$ and $\widetilde{V}_F$ are not considered, as their quantification would require additional calibration experiments. This limitation is most relevant for the RSD of $\widetilde{V}_L$ and $\widetilde{V}_R$, whereas the distributions of $\widetilde{\varepsilon}_b$ and $\widetilde{V}_F$ are independent of β. Nonetheless, qualitative considerations suggest that inclusion of such effects would likely reinforce the observed trends. Within the investigated range of β, the dispensed liquid volumes vary moderately ($\widetilde{V}_L \approx$ 113–222 µL), a regime in which automated LHS typically exhibit near-constant relative precision [34]. In contrast, increasing β necessarily reduces $\widetilde{V}_R$ to only a few microliters, where accurate and reproducible dispensing of resin slurries becomes increasingly challenging [21]. As a result, the RSD of $\widetilde{V}_R$ is expected to increase with increasing β, introducing an additional β-dependent contribution to the propagated uncertainty. Accounting for this effect would further penalize large β values and reinforce the predicted reduction in $\widetilde{K}_p$ uncertainty at lower β values.

From a design perspective, these findings define phase ratio selection as an optimization problem balancing measurement precision against material consumption. Lower β values markedly improve analytical precision but require increased protein mass, whereas higher β values reduce material demand at the expense of elevated uncertainty. The framework therefore enables direct visualization of this trade-off by jointly reporting the predicted $\widetilde{K}_p$ uncertainty and the corresponding protein demand per 96-well plate for each β (Fig. 7). In the present HTS case, protein requirements span more than an order of magnitude, ranging from 2.12 mg ($\beta = 50$, $V_R = 4.412$ µL) to 54 mg ($\beta = 1$, $V_R =$ 112.5 µL). At the same time, the predicted SD of $\widetilde{K}_p$ decreases by >50% across the full range of $K_{p,ideal}$.

On this basis, application-dependent recommendations for phase-ratio selection can be directly derived. For early-stage resin and condition screening, where relative ranking rather than absolute K_p accuracy is required and protein availability is often severely limited, higher β values in the range of ≈ 20 offer a practical compromise for the presented HTS workflow. They combine low material demand and acceptable precision, while avoiding impractically small resin volumes. For applications requiring high quantitative fidelity (mechanistic modeling and downstream column-scale predictions) the uncertainty analysis strongly favors operating at low β values to minimize propagated error in $\widetilde{K}_p$. However, this preference must be balanced against physicochemical feasibility constraints. As shown by Ram et al [39], phase ratios below approximately $\beta \approx 4$ may violate the limit of detection or isotherm-linearity criteria, leading to systematic bias rather than

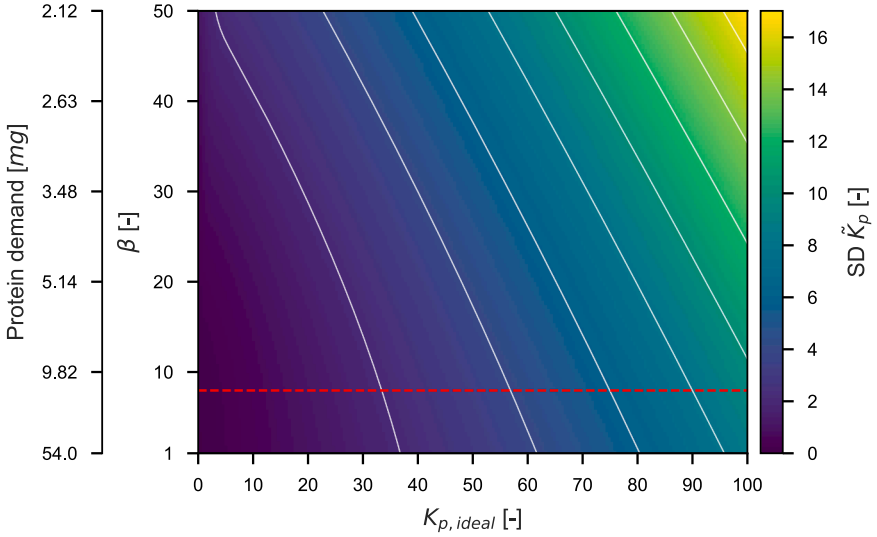

Fig. 7. Response surface of the predicted standard deviation of $\widetilde{K}_p$ as a function of the ideal chromatographic partition coefficient $K_{p,ideal}$ and the phase-ratio β. Color encodes the Monte-Carlo-derived standard deviation for each ($K_{p,ideal}$, β) combination. The corresponding protein mass demand per 96-well plate is shown on the secondary y-axis as a function of β. The red dashed line indicates the β used in the POROS XS experimental case study.

mere random error. Accordingly, optimal designs for high-precision applications are found near the lower boundary of the feasible operating regime, typically in the range $\beta \approx 4$–8, where measurement precision is maximized without compromising validity. This corresponds to a 20–70% reduction in the SD of $\widetilde{K}_p$ across the $K_{p,ideal}$ range (β=20 to β=5).

5. Conclusion

Filter-plate-based high-throughput screening of the chromatography partition coefficient K_p is widely used in purification process development, yet quantitative guidance on how experimental uncertainty propagates across the relevant equilibrium range and how it can inform assay design has been lacking.

Here, we developed and validated an experimentally calibrated Monte Carlo uncertainty-propagation framework that quantifies total uncertainty in a filter-plate-based K_p screening on a Tecan Fluent LHS and decomposes it into parameter-specific contributions. Parameter distributions of all relevant inputs to the representative workflow (liquid and slurry dispensing, hold-up parameters, and analytical readouts) were obtained from targeted characterization experiments. The model accurately reproduced the magnitude, K_p-dependent heteroscedasticity, and plate-to-plate variability observed in a mAb monomer case study on POROS XS.

Variance decomposition showed that resin slurry distribution and supernatant concentration measurements account for approximately 97% of the total variance across the investigated $K_{p,ideal}$ range. Beyond identifying dominant error sources, the framework resolves their regime-dependent relevance across the $K_{p,ideal}$ range. It further exposes a clear trade-off between measurement precision and protein demand governed by phase ratio β, enabling the derivation of application-specific phase ratio recommendations.

Importantly, the calibration effort is largely workflow- and equipment-specific. Once parameter distributions are established for a given setup (and resin format), they can be reused for subsequent proteins under identical assay conditions. Only minor adjustments are required for the UV-based concentration conversion, which depends on the protein-specific extinction coefficient.

Beyond this representative workflow, additional workflow- or equipment-specific error sources, such as pH and buffer variability, can be readily integrated into the established framework through targeted characterization when necessary. A particularly valuable extension would be the application to multi-species systems, allowing uncertainty quantification of separation factors between monomer and aggregates.

Overall, this approach transforms filter-plate-based HTS from an empirical screening tool into a quantitatively guided and design-driven methodology, providing a general basis for uncertainty-aware experimental design in chromatographic process development.

Funding

This research did not receive any specific grant from funding agencies in the public, commercial, or non-profit sectors.

CRediT authorship contribution statement

Jan Faessler: Writing – review & editing, Writing – original draft, Visualization, Validation, Software, Methodology, Investigation, Formal analysis, Data curation, Conceptualization. **Emmy Schiess:** Investigation, Data curation. **Rudger Hess:** Writing – review & editing, Supervision, Conceptualization. **Till Briskot:** Writing – review & editing, Conceptualization. **Sebastian Andris:** Writing – review & editing, Conceptualization. **Melanie Maier:** Writing – review & editing, Conceptualization. **Jan-Hendrik Huth:** Writing – review & editing, Project administration, Funding acquisition, Conceptualization. **Joey Studts:** Resources, Project administration, Funding acquisition. **Jürgen Hubbuch:** Writing – review & editing, Supervision, Conceptualization.

Declaration of competing interest

The authors declare that they have no known competing financial interests or personal relationships that could have appeared to influence the work reported in this paper.

Acknowledgements

The authors would like to thank the department of Global Development CMC Biologicals (Boehringer Ingelheim, Biberach, Germany) for enabling this project. We are especially grateful to Kristina Wösle and Selina Nalbantoglu for their support in automation. We also thank the BI DSP modeling team for their constant support and the fruitful discussions.

Supplementary materials

Supplementary material associated with this article can be found, in the online version, at doi:10.1016/j.chroma.2026.467325.

Data availability

Data will be made available on request.

References

[1] A.S. Rathore, H. Winkle, Quality by design for biopharmaceuticals, Nat. Biotechnol. 27 (2009) 26–34, https://doi.org/10.1038/nbt0109-26.
[2] M.F. Higgins, N. Abu-Absi, E. Gontarz, I.H. Gorr, K. Kaiser, P. Patel, F. Ritacco, P. Sheehy, B. Thangaraj, T. Gill, Accelerated CMC workflows to enable speed to clinic in the COVID-19 era: a multi-company view from the biopharmaceutical industry, Biotechnol. Prog. 39 (2023) e3321, https://doi.org/10.1002/btpr.3321.
[3] D.W. Wood, I. Gierach, Bioprocessing, bioengineering and process chemistry in the biopharmaceutical industry, using chemistry and bioengineering to improve the performance of biologics, (2024) 533–552. 10.1007/978-3-031-62007-2_19.
[4] S.M. Pirrung, M. Ottens, Preparative chromatography for separation of proteins, 2017, pp. 269–291, https://doi.org/10.1002/9781119031116.ch9.
[5] K.M. Łącki, High throughput process development in biomanufacturing, Curr. Opin. Chem. Eng. 6 (2014) 25–32, https://doi.org/10.1016/j.coche.2014.08.004.
[6] S.M. Cramer, M.A. Holstein, Downstream bioprocessing: recent advances and future promise, Curr. Opin. Chem. Eng. 1 (2011) 27–37, https://doi.org/10.1016/j.coche.2011.08.008.
[7] W.D. Chen, X.Y. Dong, Y. Sun, Analysis of diffusion models for protein adsorption to porous anion-exchange adsorbent, J. Chromatogr. A 962 (2002) 29–40, https://doi.org/10.1016/s0021-9673(02)00466-1.
[8] P. McDonald, B. Tran, C.R. Williams, M. Wong, T. Zhao, B.D. Kelley, P. Lester, The rapid identification of elution conditions for therapeutic antibodies from cation-exchange chromatography resins using high-throughput screening, J. Chromatogr. A 1433 (2016) 66–74, https://doi.org/10.1016/j.chroma.2015.12.071.
[9] G. Carta, Predicting protein dynamic binding capacity from batch adsorption tests, Biotechnol. J. 7 (2012) 1216–1220, https://doi.org/10.1002/biot.201200136.
[10] J.P. Welsh, S.H. Altern, J.Y. Lyall, S. Burgess, M.A. Rauscher, A.M. Lenhoff, S. M. Cramer, C. Williams, Coupling high-throughput and modeling approaches to streamline early-stage process development for biologics, Biotechnol. Prog. 41 (2025) e3523, https://doi.org/10.1002/btpr.3523.
[11] J.K. Lorek, H.S. Karkov, F. Matthiesen, M. Dainiak, High throughput screening for rapid and reliable prediction of monovalent antibody binding behavior in flowthrough mode, Biotechnol. Bioeng. 121 (2024) 2332–2346, https://doi.org/10.1002/bit.28572.
[12] M. Bensch, P.S. Wierling, E. von Lieres, J. Hubbuch, High throughput screening of chromatographic phases for rapid process development, Chem. Eng. Technol. 28 (2005) 1274–1284, https://doi.org/10.1002/ceat.200500153.
[13] T.C. Silva, M. Eppink, M. Ottens, Automation and miniaturization: enabling tools for fast, high-throughput process development in integrated continuous biomanufacturing, J. Chem. Technol. Biotechnol. 97 (2022) 2365–2375, https://doi.org/10.1002/jctb.6792.
[14] S. Chhatre, N.J. Titchener-Hooker, Review: microscale methods for high-throughput chromatography development in the pharmaceutical industry, J. Chem. Technol. Biotechnol. 84 (2009) 927–940, https://doi.org/10.1002/jctb.2125.
[15] S. Konstantinidis, S. Kong, N. Titchener-Hooker, Identifying analytics for high throughput bioprocess development studies, Biotechnol. Bioeng. 110 (2013) 1924–1935, https://doi.org/10.1002/bit.24850.

[16] J.L. Coffman, J.F. Kramarczyk, B.D. Kelley, High-throughput screening of chromatographic separations: I. method development and column modeling, Biotechnol. Bioeng. 100 (2008) 605–618, https://doi.org/10.1002/bit.21904.
[17] K.M. Lacki, E. Brekkan, High throughput screening techniques in protein purification, Methods Biochem. Anal. 54 (2011) 489–506.
[18] T. Bergander, K.M. Lacki, High-throughput process development: chromatography media volume definition, Eng. Life Sci. 16 (2016) 185–189, https://doi.org/10.1002/elsc.201400240.
[19] T. Herrmann, M. Schröder, J. Hubbuch, Generation of equally sized particle plaques using solid-liquid suspensions, Biotechnol. Prog. 22 (2006) 914–918, https://doi.org/10.1021/bp050296i.
[20] G. Barker, J. Calzada, Z. Ouyang, N. Domagalski, S. Herzer, S. Rieble, A systematic approach to improve data quality in high-throughput batch adsorption experiments, Eng. Life Sci. 16 (2016) 124–132, https://doi.org/10.1002/elsc.201400242.
[21] J. Kittelmann, M. Ottens, J. Hubbuch, Robust high-throughput batch screening method in 384-well format with optical in-line resin quantification, J. Chromatogr. B 988 (2015) 98–105, https://doi.org/10.1016/j.jchromb.2015.02.028.
[22] X. Li, G. de Roo, K. Burgers, M. Ottens, M. Eppink, Self-packed filter plates: a good alternative for pre-packed filter plates for developing purification processes for therapeutic proteins, Biotechnol. J. 7 (2012) 1269–1276, https://doi.org/10.1002/biot.201200045.
[23] W. Wiechert, L.M. Helleckes, K. Nöh, Building trust in automated experimentation: uncertainty quantification in the era of high-throughput biolabs, Curr. Opin. Biotechnol. 96 (2025) 103382, https://doi.org/10.1016/j.copbio.2025.103382.
[24] H. Alosert, J. Savery, J. Rheaume, M. Cheeks, R. Turner, C. Spencer, S.S. Farid, S. Goldrick, Data integrity within the biopharmaceutical sector in the era of Industry 4.0, Biotechnol. J. 17 (2022) e2100609, https://doi.org/10.1002/biot.202100609.
[25] A. Maier, M. Cha, S. Burgess, A. Wang, C. Cuellar, S. Kim, N.S. Rajan, J. Neyyan, R. Sengupta, K. O'Connor, N. Ott, A. Williams, Predicting purification process fit of monoclonal antibodies using machine learning, mAbs 17 (2025), https://doi.org/10.1080/19420862.2024.2439988, 2024.08.05.606711.
[26] M. Hartmann, M. Rauscher, J. Robinson, J. Welsh, D. Roush, Integration of QSAR models with high throughput screening to accelerate the development of polishing chromatography unit operations, J. Chromatogr. A 1747 (2025) 465818, https://doi.org/10.1016/j.chroma.2025.465818.
[27] J.C. for G. in Metrology., Evaluation of measurement data — supplement 1 to the "Guide to the expression of uncertainty in measurement" — propagation of distributions using a Monte Carlo method, (2008).
[28] L.M. Helleckes, M. Osthege, W. Wiechert, E. von Lieres, M. Oldiges, Bayesian calibration, process modeling and uncertainty quantification in biotechnology, PLoS Comput. Biol. 18 (2022) e1009223, https://doi.org/10.1371/journal.pcbi.1009223.
[29] W. Heymann, J. Glaser, F. Schlegel, W. Johnson, P. Rolandi, E. von Lieres, Advanced error modeling and bayesian uncertainty quantification in mechanistic liquid chromatography modeling, J. Chromatogr. A 1708 (2023) 464329, https://doi.org/10.1016/j.chroma.2023.464329.
[30] T. Briskot, F. Stückler, F. Wittkopp, C. Williams, J. Yang, S. Konrad, K. Doninger, J. Griesbach, M. Bennecke, S. Hepbildikler, J. Hubbuch, Prediction uncertainty assessment of chromatography models using bayesian inference, J. Chromatogr. A 1587 (2019) 101–110, https://doi.org/10.1016/j.chroma.2018.11.076.
[31] A.S. Kurup, H.J. Subramani, M.T. Harris, A Monte Carlo-based error propagation analysis of simulated moving Bed systems, Sep. Purif. Technol. 62 (2008) 582–589, https://doi.org/10.1016/j.seppur.2008.02.021.
[32] E. Hund, D.L. Massart, J. Smeyers-Verbeke, Comparison of different approaches to estimate the uncertainty of a liquid chromatographic assay, Anal. Chim. Acta 480 (2003) 39–52, https://doi.org/10.1016/s0003-2670(02)01591-x.
[33] D.B. Hibbert, J. Jiang, M.I. Mulholland, Propagation of uncertainty in high-performance liquid chromatography with UV–VIS detection, Anal. Chim. Acta 443 (2001) 205–214, https://doi.org/10.1016/s0003-2670(01)01222-3.
[34] A. Osberghaus, P. Baumann, S. Hepbildikler, S. Nath, M. Haindl, E. von Lieres, J. Hubbuch, Detection, quantification, and propagation of uncertainty in high-throughput experimentation by Monte Carlo methods, Chem. Eng. Technol. 35 (2012) 1456–1464, https://doi.org/10.1002/ceat.201100610.
[35] B.D. Kelley, M. Switzer, P. Bastek, J.F. Kramarczyk, K. Molnar, T. Yu, J. Coffman, High-throughput screening of chromatographic separations: IV. Ion-exchange, Biotechnol. Bioeng. 100 (2008) 950–963, https://doi.org/10.1002/bit.21905.
[36] B.D. Kelley, S.A. Tobler, P. Brown, J.L. Coffman, R. Godavarti, T. Iskra, M. Switzer, S. Vunnum, Weak partitioning chromatography for anion exchange purification of monoclonal antibodies, Biotechnol. Bioeng. 101 (2008) 553–566, https://doi.org/10.1002/bit.21923.
[37] E.E. Brumbaugh, G.K. Ackers, Molecular sieve studies of interacting protein systems VII. Direct optical scanning method for ligand-macromolecule binding studies, Anal. Biochem. 41 (1971) 543–559, https://doi.org/10.1016/0003-2697(71)90177-1.
[38] C.C. Shepard, A. Tiselius, The chromatography of proteins. the effect of salt concentration and pH on the adsorption of proteins to silica gel, Discuss. Faraday Soc. 7 (1949) 275, https://doi.org/10.1039/df9490700275.
[39] J. Ram, M. Snyder, C. Belisle, S. Koley, N. Vecchiarello, Defining operating regimes for partition coefficient measurements in protein chromatography, J. Chromatogr. A 1745 (2025) 465730, https://doi.org/10.1016/j.chroma.2025.465730.
[40] J. Gong, Galton Board experiment: proof of central limit theorem, Sci. Technol. Eng. Chem. Environ. Prot. 1 (2025), https://doi.org/10.61173/j4y96z15.
[41] J.F. Ogilvie, A Monte-Carlo approach to error propagation, Comput. Chem. 8 (1984) 205–207, https://doi.org/10.1016/0097-8485(84)80007-8.
[42] S.Y. Kim, D.W. Shin, J. Hyun, N.H. Kwon, J.C. Cheong, K.J. Paeng, J. Lee, J.Y. Kim, Uncertainty evaluation for the quantification of urinary amphetamine and 4-hydroxyamphetamine using liquid chromatography–tandem mass spectrometry: comparison of the guide to the expression of uncertainty in measurement approach and the Monte Carlo method with R, Molecules 28 (2023) 6803, https://doi.org/10.3390/molecules28196803.
[43] A. Saltelli, M. Ratto, T. Andres, F. Campolongo, J. Cariboni, D. Gatelli, M. Saisana, S. Tarantola, Global sensitivity analysis, Primer (2023), https://doi.org/10.1002/9780470725184.
[44] A. Biwer, S. Griffith, C. Cooney, Uncertainty analysis of penicillin V production using Monte Carlo simulation, Biotechnol. Bioeng. 90 (2005) 167–179, https://doi.org/10.1002/bit.20359.
[45] H. Verbeeck, R. Samson, F. Verdonck, R. Lemeur, Parameter sensitivity and uncertainty of the forest carbon flux model FORUG: a Monte Carlo analysis†, Tree Physiol. 26 (2006) 807–817, https://doi.org/10.1093/treephys/26.6.807.
[46] S.S. Shapiro, M.B. Wilk, An analysis of variance test for normality (complete samples)†, Biometrika 52 (1965) 591–611, https://doi.org/10.1093/biomet/52.3-4.591.
[47] M.B. Wilk, R. Gnanadesikan, Probability plotting methods for the analysis of data, Biometrika 55 (1968) 1–17, https://doi.org/10.1093/biomet/55.1.1.
[48] R.D. Gosselin, Testing for normality: a user's (cautionary) guide, Lab. Anim. 58 (2024) 433–437, https://doi.org/10.1177/00236772241276808.
[49] M.T. Alexander, D.C. Montgomery, G. Runger, Applied statistics and probability for engineers, Technometrics 37 (1995) 455, https://doi.org/10.2307/1269738.
[50] E.L. McGown, D.G. Hafeman, Multichannel pipettor performance verified by measuring pathlength of reagent dispensed into a microplate, Anal. Biochem. 258 (1998) 155–157, https://doi.org/10.1006/abio.1998.2621.
[51] H. Schmidt-Traub, M. Schulte, A. Seidel-Morgenstern, Preparative chromatography, 2020, https://doi.org/10.1002/9783527816347.
[52] L. Sooväli, E.I. Rõõm, A. Kütt, I. Kaljurand, I. Leito, Uncertainty sources in UV-vis spectrophotometric measurement, Accreditation Qual. Assur. 11 (2006) 246–255, https://doi.org/10.1007/s00769-006-0124-x.
[53] S. Kreusch, S. Schwedler, B. Tautkus, G.A. Cumme, A. Horn, UV measurements in microplates suitable for high-throughput protein determination, Anal. Biochem. 313 (2003) 208–215, https://doi.org/10.1016/s0003-2697(02)00460-8.
[54] T. Bergander, K. Nilsson-Välimaa, K. Öberg, K.M. Lacki, High-throughput process development: determination of dynamic binding capacity using microtiter filter plates filled with chromatography resin, Biotechnol. Prog. 24 (2008) 632–639, https://doi.org/10.1021/bp0704687.
[55] S. Lilyanna, E.M.W. Ng, S. Moriguchi, S.P. Chan, R. Kokawa, S.H. Huynh, P.C. J. Chong, Y.X. Ng, A.M. Richards, T.W. Ng, O.W. Liew, Variability in microplate surface properties and its impact on ELISA, J. Appl. Lab. Med. 2 (2018) 687–699, https://doi.org/10.1373/jalm.2017.023952.
[56] E.L. McGown, UV absorbance measurements of DNA in microplates, BioTechniques 28 (2000) 60–64, https://doi.org/10.2144/00281bm11.